Bridging knowledge gaps with hybrid machine-learning forest ecosystem models (ML-FEMs): inferential simulation of past understory light regimes

Adam Erickson[1,†*], Craig Nitschke[2]

[1]Integrated Remote Sensing Studio, Department of Forest Resources Management, University of British Columbia, 2045-2424 Main Mall, Vancouver, British Columbia, V6T 1Z4, Canada

[2]School of Ecosystem and Forest Sciences, University of Melbourne, 500 Yarra Boulevard, Richmond, Victoria, 3121, Australia

[†]*Current address*: Hydrological Sciences Laboratory, Code 617, NASA Goddard Space Flight Center, 8800 Greenbelt Road, Greenbelt, Maryland, 20771, USA

[*]Corresponding author: adam.michael.erickson@gmail.com

ORCID: 0000-0002-8730-073X

Twitter: @admercs

Non-peer-reviewed pre-print submitted to EarthArXiv

Keywords: hybrid land models; machine learning; forest ecosystem models; ecological modeling; pattern-based process models; data-driven

Abstract

Soil moisture is a key limiting factor of plant productivity in boreal and montane regions, producing additional climate feedbacks through evaporation, regeneration, mortality, and respiration. Understory solar irradiation – the primary driver of surface temperature and evaporative demand – remains poorly represented in vegetation models due to a lack of 3-D canopy geometry. Existing models are further unable to represent processes lacking sufficient parameterization and/or knowledge, with no land model to date utilizing machine learning (ML) to represent vegetation processes. Here, we developed the first hybrid forest ecosystem model using ML (ML-FEM), a specific case of hybrid AI land model (a concept also invented here). In this approach, ML models are trained and validated with a ground-truth dataset, whether observations or high-fidelity simulations, before being applied to vegetation model parameters for inference, internally or externally to the model. Using this approach, we simulated annual understory global solar irradiation (I_u) across 25.2 Mha in southwestern Canada at 1-ha resolution under historical climate and fire scenarios. In cross-validation, we found that linear and ML regression models performed comparably well in the prediction of angular canopy cover (ACC), due to the linearity of its relationship to predictors (linear R^2 = 0.938, RMSE = 0.079; ML R^2 = 0.939, RMSE = 0.074). Reduced area burned, increased ignitions, and reduced regeneration potential for recent periods resulted in stable or reduced I_u. This suggests that diminished disturbance may reduce I_u through forest aging, masking latent regeneration decline. Only in the most extreme and unconstrained scenarios did I_u increase. In these experiments, conducted in late 2015, we demonstrated an entirely new class of hybrid models that we anticipated to be of vital importance to understanding and representing pattern-based processes in Earth system models.

Introduction

Light is a primary source of life for plants, as its physical energy drives the process of photosynthesis, making light a focus of plant resource competition (Hikosaka & Hirose, 1997; Katahata, Naramoto, Kakubari, & Mukai, 2005; Ruban, 2009). This include phototropism and a range of life history strategies linked to metabolic limitations per the leaf/plant economics spectrum (Enquist & Niklas, 2001; Wright et al., 2004; Enquist, West, & Brown, 2009). While plants have evolved adaptations that enable them to tolerate fluctuations in the understory light environment (Chazdon & Pearcy, 1991; Way & Pearcy, 2012), long-term light changes may affect succession through game-theoretic shade tolerance, growth, and regeneration strategies. Understory global solar irradiation (I_u) (i.e., the kinetic energy of photons incident across the sky hemisphere integrated over time and space) exerts a control on biogeochemical and energetic budgets through its effects on evaporative demand and soil moisture (Farquhar & Roderick, 2009).

Global solar irradiation (I) represents the sum of direct, diffuse, and reflected solar irradiation components. Direct and diffuse radiation comprise the majority of the insolation budget (Iqbal, 1983). While direct radiation theoretically reaches the surface unimpeded, diffuse radiation is scattered by molecules in the atmosphere, and reflected radiation is returned by surface features. Although only a fraction of incident radiation can be used by plants in photosynthesis, known as the fraction of photosynthetically active radiation (fPAR or fAPAR), full-spectrum changes to radiation regimes are important in determining changes to energy balance (Paul M Rich, 1990) and thus changes to evaporative demand and soil water.

Understory plants are believed to play a central role in processes from tree regeneration (Greene et al., 1999) and nutrient cycling to fire frequency, with some suggesting that understory dynamics drive stand succession (Nilsson & Wardle, 2005). Previous studies have shown the importance of I_u in maintaining the diversity and productivity of understory plants in boreal forests (Aubin, Beaudet, & Messier, 2000; Grandin, 2004; Bartemucci, Messier, & Canham, 2006; Beaudet et al., 2011; Reich, Frelich, Voldseth, Bakken, & Adair, 2012; Pec et al., 2015), making I_u critical to the habitat of brown bear (*Ursus arctos*) and other boreal fauna. Improving our understanding of understory light dynamics is a key area of inquiry for scientists and managers (Lieffers, Messier, Stadt, Gendron, & Comeau, 1999). Canopy geometry, topography, and seasonality strongly affect understory light conditions. High latitude forests are characterized by narrow tree crowns, likely a population-level evolutionary adaptation to low solar elevations. While forest structure or geometry (e.g., due to thinning or disturbance) exerts direct influence on canopy light transmission (Lieffers et al., 1999; Beaudet & Messier, 2002; Bartemucci et al., 2006), or T, variation may be generalized to species-age cohort classes (Canham, Finzi, Pacala, & Burbank, 1994).

While increased understory solar irradiation and temperatures may be beneficial to boreal understory plant production, given parallel increases to precipitation (Trenberth, 2011) and atmospheric CO_2, long-term increases in evaporative demand may diminish soil water, limiting understory regeneration and growth potential (Adam M. Erickson, Nitschke, Coops, Cumming, & Stenhouse, 2015; D'Orangeville et al., 2018). Although boreal understory dynamics remain poorly understood, recent work in the Swedish boreal attributed an observed reduction in soil water to increased I_u (Grandin, 2004). Yet, the quality rather than quantity of light may be more important to long-term growth (Dengel & Grace, 2010). An improved understanding of I_u will facilitate the prediction of evaporative demand and thus soil water levels (Farquhar & Roderick, 2009), a primary limiting factor of productivity in the southern boreal (Adam M. Erickson et al., 2015; D'Orangeville et al., 2018).

While passive spaceborne remote sensing shows promise for large-area characterization of soil moisture (Laskin, Montaghi, Nielsen, & McDermid, 2016), it remains difficult to simulate as it is a pattern-based physical process sensitive to scale effects and difficult-to-map variation in belowground composition. While physical-geometric models with detailed canopy geometries – such as 3-D procedural or stochastic L-systems tree models – may be ideal for physical models of soil moisture, their computational expense and parameterization requirements remain inhibitive for large-scale simulations.

Fire plays a primary role in regulating forest structure and composition in circumpolar boreal forests (Rowe & Scotter, 1973). The evolution of boreal ecosystems was shaped by large stand-replacing fires, temperature extremes coupled to strong seasonality of the light environment, and geomorphological processes related to glaciation (Rowe, 1973; He, Pausas, Belcher, Schwilk, & Lamont, 2012). Warming has produced complex interactions between fire, productivity, and regeneration in regions of the boreal region of Alberta, Canada (Adam M. Erickson et al., 2015). Here, we simulate the combined effects of fire and climate on understory light conditions across western Alberta. We hypothesized that a climatically-driven reduction in tree regeneration potential (Adam M. Erickson et al., 2015) will reduce the forested area and increase understory global solar irradiation (I_u) given the persistence of observed 20th century climate and fire trends. Our experimental design reduces uncertainty by discarding climate projections and instead focusing on observed historical patterns applied to an initial state of year 2000 conditions. This serves as a *Gedankenexperiment* regarding the stability of a year 2000 landscape given the persistence of 20th century trends.

Materials and methods

We modeled the combined effects of canopy structure, topography, and Earth-sun geometry on understory solar irradiation (I_u), demonstrating a new class of pattern-based hybrid vegetation model based on machine learning (Adam Michael Erickson, 2017). We developed and applied statistical or empirical regression models of canopy gap fraction (P_o = 1 – ACC) to simulate a complex pattern-based process poorly represented in the LANDIS-II model: I_u. We multiplied the resulting values for P_o at each simulation time-step by corresponding physical-topographic model bare-Earth insolation values to dynamically simulate changes to I_u, providing a hybrid statistical-physical model of understory light that can be used in forecasting applications.

This work began with an exploration of regression models of angular canopy closure (ACC) developed with 1 ha (100 m^2) airborne laser scanning (ALS) plot data at field inventory sites in western Alberta (n = 100), established for brown bear (*Ursus arctos*) habitat research (Nielsen, 2005). Ground measurements of ACC recorded with a convex spherical densiometer were used to train and cross-validate ALS linear and machine-learning regression models of ACC. We decided that including ALS models of ACC was an unnecessary step, as ground-based models of ACC alone would suffice for our task. Thus, we pursued an alternate methodology that only relied upon ground-truth measurements to reduce error propagation in ACC models, even if the ALS data provide greater sampling density than convex spherical densiometers. We leave discussion of implicit biases toward ground-sampled data as the ‘ground-truth’ for another paper.

We simulated landscape I_u using a hybrid modeling approach combining the LANDIS-II forest landscape model (Scheller et al., 2007), the TACA biophysical tree regeneration model

(Nitschke & Innes, 2008; Adam M. Erickson et al., 2015), a physically-based solar radiation model (Fu & Rich, 1999), and two types of regression model: multiple-linear and machine learning. Models of processes learned from data require that the parameter vector of predictors be available in both the field data and the simulation model, or that these variables can be modeled using surrogates predicted with other variables; the former is needed for training while the latter is needed for inference (i.e., applying trained or calibrated models to generate predictions). Thus, a key practical challenge in applying our proposed ML-FEM approach is finding sets of field and model data that intersect for the process and spatiotemporal resolution of interest; this includes any potential remote sensing data streams.

We trained and cross-validated multiple-linear and machine-learning regression models of ACC using convex spherical densiometer measurements (n = 950) for the Rocky Mountain Foothills region near Hinton, Alberta, Canada. We used 10-fold cross-validation repeated three times for each model, randomly selecting 75% of the data for model training and 25% for model testing in cross-validation. Root-mean-squared error (RMSE) and coefficient of determination (R^2) metrics were used to select final regression models. We ran four model scenarios to simulate landscape-level changes to ACC: Pre-suppression Era (1923-1952); Early Suppression Era (1953-1982), Global Change Era (1983-2012); and, Most Recent Decade (2003-2012). Landcover classification was performed on LANDIS-II model outputs using the ABMI Landcover 2010 scheme (Alberta Biodiversity Monitoring Institute, 2012) for the application of the trained ACC models in inference. Next, we applied a physical-topographic global solar irradiation model to simulate landscape-level changes to insolation I_u by multiplying modeled P_o (1 – ACC) and bare-Earth insolation maps.

We assessed the effects of historical climate and fire patterns on landscape-scale I_u using a factorial experiment that included results from two contrasting classes of fire model: empirical and semi-mechanistic. For both fire models, we applied a new type of approximate stochastic gradient descent (Widrow & Hoff, 1960) that we previously proposed (Erickson et al., *in review*), characterized by the optimization of low-resolution model runs followed by full-resolution optimization for final parameter refinement, markedly improving model fit ($\overline{R^2}$= 0.96; $\overline{\Delta R^2}$ = +0.14; Supplementary Materials). Model simulations were run for a 50-year duration at annual resolution, treating the first 10 years of the simulation as the model spin-up period. We made no assumptions regarding the equilibrium state of existing vegetation communities; vegetation communities were not assumed to be in equilibrium and the model was not used to estimate equilibrium vegetation, as our study focuses on the 50-year period in order to balance initial conditions and model behavior. Further methodological details are provided below.

Data

Plot data used for the development of regression models include area-based canopy and terrain airborne laser scanning (ALS) metrics calculated with USDA Fusion (McGaughey, 2014), 30-year normal climate variables output from ClimateWNA (Wang, Hamann, Spittlehouse, & Murdock, 2011), Alberta Wet Areas maps derived from ALS data (Arp, Castonguay, Campbell, & Hiltz, 2009), Alberta Biodiversity Monitoring Institute (ABMI) Landcover 2010, Canada Land Inventory (CLI) forest site index, bare-Earth insolation calculated in ArcGIS, NASA SRTM digital elevation model (DEM), and ground-level GPS coordinates and vegetation survey data (Nielsen, 2005). The overall plot data included the following 58 variables:

Easting, northing, elevation, graminoid abundance, ALS return count, ALS height maximum, ALS height mean, ALS height 5th percentile, ALS height 10th percentile, ALS height 25th percentile, ALS height 50th percentile, ALS height 75th percentile, ALS height 90th percentile, ALS height 95th percentile, ALS ratio of returns above 2m, ALS ratio of returns above mean return height, ALS height relative ratio, ALS height skewness, ALS height standard deviation, ALS terrain aspect, ALS terrain slope, ALS terrain elevation, ALS terrain, ALS terrain plan curvature, ALS terrain profile curvature, ALS terrain solar index, wet areas, convex spherical densiometer ACC, percent conifer, regeneration, degree-days below 0, frost days, frost-free period, growing season precipitation, mean annual precipitation, monthly maximum temperature, monthly minimum temperature, July mean temperature, March precipitation, product of May × September precipitation, June precipitation, December precipitation, summer heat moisture index, January minimum temperature, July minimum temperature, herbaceous plant abundance, ABMI landcover, CLI forest site index, shrub abundance, diffuse radiation, global radiation, product of June × August global solar radiation, product of June × September global solar radiation, ALS compound topographic index (CTI), CTI 150m, CTI 90m, topographic position index, ALS canopy equation

Example maps of variables used in the regression analysis are provided below, including ClimateWNA 1961-1990 mean July precipitation and minimum January temperature, and modeled bare-Earth global solar irradiation (Figure 1). The physically-based model used to calculate bare-Earth solar irradiation (*I*) is described in a subsequent section.

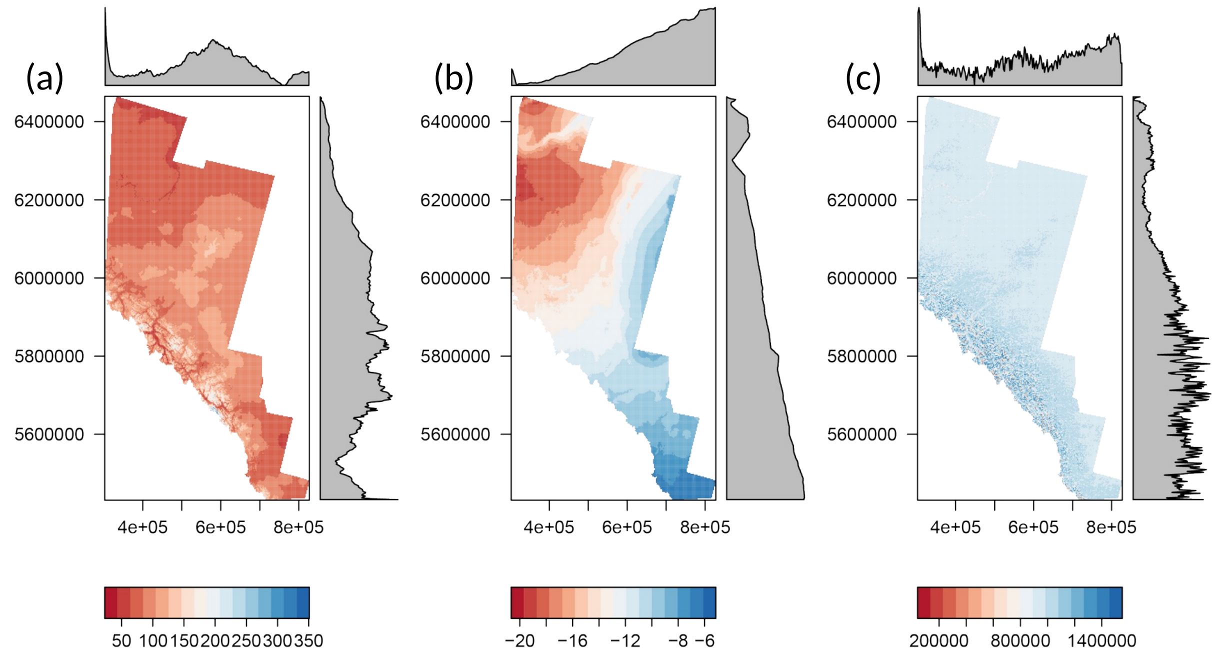

Figure 1. Predictor variable maps for the study area: (a) 1961-1990 mean July precipitation in mm; (b) 1961-1990 minimum January temperature in degrees C; (c) mean annual bare-Earth global solar irradiation in Wh m^{-2} $year^{-1}$; axis values represent pixel coordinates in NAD83 UTM 11N (meters) coordinates, used for its high positional accuracy at regional scales

Linear and machine learning regression models of P_o

Multivariate linear regression follows the classical form:

$$y_i = \beta_1 x_{i1} + \cdots + \beta_p x_{ip} + \varepsilon_i = X_i^T \beta + \varepsilon_i \, for \, i = 1 \ldots n$$

Where T denotes the transpose, such that $X_i^T \beta$ is the inner product between x_i and weight vector β. The ordinary least squares method was used to solve for weights and the intercept term that minimizes error. The Random Forest implementation also follows this classical form (Leo Breiman, 2001) based on the construction of forests of decision trees, described in the following section. The effects of predictor variables on model performance for both types of model were tested. For linear regression, this was done with step-wise AIC and BIC model selection, as well as manual variable selection based on an analysis of variance and logical deduction regarding dynamics related to variation in P_o. For Random Forest models, variable selection was based on variable importance per the mean decrease in accuracy.

The Random Forest algorithm

The Random Forest algorithm (Leo Breiman, 2001) builds on the bagging procedure (i.e., bootstrap aggregation), or the averaging of many noisy unbiased models to reduce variance by building a large collection or forest of de-correlated regression trees before performing averaging (L Breiman, 1996). Decision trees are ideal for bagging procedures, as they capture complex interactions and, have low bias and high noise (Hastie, Tibshirani, & Friedman, 2009). The bias of bagged trees is identical to that of individual trees, making variance the focus of improvement. Random Forest was designed to improve the variance reduction of bagging by minimizing the correlation between trees without substantially increasing the variance. This is achieved by randomly selecting input variables during the tree-growing process. The Random Forest algorithm is further described below (Algorithm 1), adopted from Hastie *et al.* (2009).

Algorithm 1: Random Forest Algorithm for Regression or Classification

1. For b = 1 to B:
   a. Draw a bootstrap sample Z* of size *N* from the training data
   b. Grow a random-forest tree T_b to the bootstrapped data, by recursively repeating the following steps for each terminal node of the tree, until the minimum node size n_{min} is reached
      i. Select *m* variables at random from the *p* variables
      ii. Pick the best variable/split-point among the *m*
      iii. Split the node into two daughter nodes
2. Output the ensemble of trees $\{T_b\}_1^B$

Following model training, to make a prediction at a new point *x*:

Regression: $\hat{f}_{rf}^{B}(x)=\frac{1}{B}\sum_{b=1}^{B} T_b(x)$

Classification: Let $\hat{C}_b(x)$ be the class prediction of the *b*th Random Forest tree. Then,

$$\hat{C}_{rf}^{B}(x)=majority\ vote\{\hat{C}_b(x)\}_1^B$$

In short, the Random Forest algorithm creates *n-trees* decision trees from randomly selected variables with *mtry* splits at each node. Each of these trees is a weak predictor, combined through averaging to produce predictions. Here, we focus on the regression case.

Landcover classification of LANDIS-II species-age cohorts

To simulate P_o (1 – ACC) at the landscape scale using the LANDIS-II model, we classified simulated annual species-age cohorts into landcover classes per the ABMI Wall-to-wall Landcover Map 2010 Version 1.0 scheme (Alberta Biodiversity Monitoring Institute, 2012). The following section describes the lookup table (Table 1) and algorithm (Algorithm 2) used for classifying simulated species-age cohorts into ABMI landcover classes for pixels/sites, providing landcover maps at annual resolution.

Table 1. ABMI Landcover 2010 classification scheme

Value	Landcover Class
0	None
20	Water
31	Snow/Ice
32	Rock/Rubble
33	Exposed Land
34	Developed
50	Shrubland
110	Grassland
120	Agriculture
210	Evergreen (Coniferous) Forest
220	Broadleaf Forest
230	Mixed Forest

The algorithm we developed and applied to classify species-age cohorts into ABMI landcover classes is described in further detail below (Algorithm 2).

Algorithm 2: Classification of LANDIS-II species-age cohorts into ABMI landcover classes

1. For each LANDIS-II simulation scenario:
    a. For each simulation year:
        i. For each species-age map:
            1. Assign pixels to either evergreen or broadleaf classes
        ii. Count the number of species present for each class
        iii. Calculate richness as the sum of species present per class
        iv. Calculate percent evergreen/broadleaf by dividing by species richness
        v. Classify pixels inactive in LANDIS-II simulations to remove pixels masked in the simulations:
            1. Use ABMI Landcover 2010 map to assign values for classes 0-120
        vi. Classify pixels active in LANDIS-II simulations, overwriting previous classification values for sites that fail to regenerate post-disturbance:
            1. Assign pixels to Evergreen Forest (210) where greater than 75%
            2. Assign pixels to Broadleaf Forest (220) where greater than 75%
            3. Assign pixels to Mixed Forest (230) where both percent evergreen and broadleaf are greater than or equal to 25%
            4. Assign pixels to Grassland (110) where both percent evergreen and broadleaf are equal to zero
    b. Save landcover time-series to disk for use in regression models of P_o

Simulated species-age cohorts were classified taxonomically into needleleaf-evergreen or broadleaf binary classes; deciduous-needleleaf *Larix* species were classified as evergreen per the

ABMI scheme. The sum of binary presence values for each pixel/site and taxonomic group was calculated in order to determine the fraction of evergreen-to-broadleaf species. Immature trees, assumed less than ten years of age, were filtered out to correct for transient dynamics. Standard ABMI Landcover 2010 class values were applied at pixels/sites marked as inactive in the simulations. Sites characterized by > 75% evergreen trees were classified as Evergreen Forest while sites > 75% broadleaf trees were classified as Broadleaf Forest. Sites where both evergreen and broadleaved trees represented > 25% of the site were classified as Mixed Forest. Active sites absent any tree species were classified as Grasslands to account for sites where regeneration failure occurred.

Bare-Earth global solar irradiation model

We used ArcGIS Spatial Analyst solar radiation tools (Fu & Rich, 1999) with an SRTM RADAR digital elevation model (DEM) processed using standard correction techniques to compute bare-Earth global solar irradiation across the 25.2 Mha study area at 1 ha resolution. In the following text, we provide a description of the solar radiation model used. Based on previous work (Paul M Rich, 1990; P. M. Rich, Dubayah, Hetrick, & Saving, 1994; Fu & Rich, 2002) parallel to GRASS *r.sun* algorithm development (Šúri & Hofierka, 2004), global solar radiation was calculated per the following:

1. Convert the 3-D hemispherical viewshed for a DEM cell to 2-D polar chart
2. Calculate half-hourly solar position polar chart based on solar zenith (θ) and azimuth (ϑ)
3. Calculate half-hourly direct solar radiation for sectors in a 2-D polar chart

4. Calculate half-hourly diffuse solar radiation for sectors in a 2-D polar chart
5. Calculate total direct solar radiation by masking sky sectors of (3) with pixels of (1)
6. Calculate total diffuse solar radiation by masking sky sectors of (4) with pixels of (1)
7. Calculate global solar radiation for the cell as the sum of (5) and (6)

Each 2-D polar chart shares the same projection, facilitating fast matrix computation. The computation of the hemispherical viewshed from the perspective of the ground looking toward the zenith is similar to hemispherical photography, convex spherical densiometers, and hemispherical LiDAR approaches of estimating light occlusion, making the solar model compatible with the proposed modeling framework.

The hemisphere calculations used were originally developed for hemispherical photography vegetation studies (Paul M Rich, 1990; Fu & Rich, 1999). In the viewshed calculation, twelve equal azimuth angles are searched from the pixel center for computation of the maximum horizon angle (unobstructed zenith). The horizon angles are then converted into a hemispherical coordinate system as zenith (θ) and azimuth) angle sectors of a polar plot. Each cell within the hemisphere sectors takes one of two binary values, visible or occluded.

The half-hourly sun position is calculated using standard equations (Iqbal, 1983), used for calculating direct and diffuse radiation components. The calculation of direct, diffuse, and global radiation for a given sun position follows previous work (Paul M Rich, 1990; P. M. Rich et al., 1994; Fu & Rich, 2002). Global solar irradiation (I_{global}) is the sum of direct I_{direct} and diffuse $I_{diffuse}$ components, ignoring reflected irradiation:

$$I_{global} = I_{direct} + I_{diffuse}$$

Direct solar irradiation I_{direct} is computed as the sum of irradiation for each sector defined by zenith (θ) and azimuth (ϑ) angles for each hour and month:

$$I_{direct} = \sum I_{direct_{\theta,\vartheta}}$$

The direct solar irradiation for a given zenith and azimuth angle sector is calculated as the solar constant for the mean Earth-sun distance (S_{const}), equal to 1367 W m^{-2}, multiplied by the atmospheric transmissivity for the shortest path raised to the relative optical path length (β^{m_θ}), the sky sector sun duration ($t_{\theta,\vartheta}$), equal to monthly and half-hourly intervals or spherical geometry, the gap fraction for the sun map sector ($P_{\theta,\vartheta}$), and the cosine of the angle of incidence between the sky sector centroid and the surface normal ($\gamma_{\theta,\vartheta}$):

$$I_{direct_{\theta,\vartheta}} = S_{const} * \beta^{m_\theta} * t_{\theta,\vartheta} * P_{\theta,\vartheta} * \cos\gamma_{\theta,\vartheta}$$

Relative optical path (m_θ) is calculated based on the cell elevation in meters (z) and solar zenith angle (θ):

$$m_\theta = \exp\left(-0.000118 * z - 1.638 * 10^{-9} * z^2\right) / \cos\theta$$

The angle of incidence ($\gamma_{\theta\vartheta}$) is calculated based on the solar zenith angle (θ), surface zenith angle (G_z), and surface azimuth angle (G_a):

$$\gamma_{\theta\vartheta} = \cos^{-1}\theta * \cos G_z + \sin\theta * \sin G_z * \cos(\vartheta - G_a)$$

Diffuse solar irradiation $I_{diffuse}$ is computed as the sum of irradiation for each of 128 sectors, given 8 zenith (θ) and 16 azimuth (ϑ) angle divisions:

$$I_{diffuse} = \sum I_{diffuse_{\theta,\vartheta}}$$

Unlike direct irradiation, $I_{diffuse_{\theta,\vartheta}}$ sectors are calculated as the rolling sum of half-hourly values for a given time interval, due to the multi-directional nature of diffuse radiation, with each sector predefined rather than based on modeled solar position. The diffuse solar irradiation for a given zenith and azimuth angle sector is calculated as the global normal radiation (R_{glb}) multiplied by the proportion of diffused global radiation flux ($p_{diffuse}$), time interval (t), sky sector gap fraction ($P_{\theta,\vartheta}$), weighted proportion of diffuse radiation originating from a sector ($w_{\theta,\vartheta}$), and cosine of the angle of incidence ($\gamma_{\theta,\vartheta}$):

$$I_{diffuse_{\theta,\vartheta}} = R_{glb} * p_{diffuse} * t * P_{\theta,\vartheta} * w_{\theta,\vartheta} * \cos\gamma_{\theta,\vartheta}$$

Global normal radiation (R_{glb}) is calculated as the solar constant (S_{const}) multiplied by the sum of the atmospheric transmissivity for the shortest path raised to the relative optical path length (β^{m_θ}), divided by one minus the proportion of diffused global radiation flux ($p_{diffuse}$) to correct for direct radiation:

$$R_{glb} = \left(S_{const} \sum \beta^{m_\theta} \right) / \left(1 - p_{diffuse} \right)$$

The weighted proportion of diffuse radiation originating from a sector ($w_{\theta,\vartheta}$) is calculated as the zenith angle range for a sky sector ($\cos\theta_2 - \cos\theta_1$) divided by the number of azimuth divisions in the sky map (N_ϑ):

$$w_{\theta,\vartheta} = \left(\cos\theta_2 - \cos\theta_1 \right) / N_\vartheta$$

Each of these calculations was performed for each cell in the NASA SRTM DEM using ArcGIS solar analyst tools (Fu & Rich, 1999). For more details on model parameterization, please refer to the Supplementary Materials.

Results

Our hybrid model simulation results showed that I_u levels increased as the forested area declined. Multivariate-linear and machine-learning (ML) regression models of ACC using the Random Forest algorithm showed comparable performance. Both types of regression model performed well using only two predictor variables, Alberta Biodiversity Monitoring Institute (ABMI) Landcover 2010 and Canada Land Inventory (CLI) Forest Site Index. Multiple-linear regression with step-wise AIC produced excellent model fit (multiple and adjusted $R^2 = 0.949$; $RMSE = 0.067$), selecting 25 predictor variables. Step-wise BIC produced comparable results (multiple and adjusted $R^2 = 0.946$; $RMSE = 0.069$) while selecting only 9 predictor variables. An analysis of variance (ANOVA) for all predictors informed the selection of two predictors logically complementary in their ability to predict P_o: ABMI Landcover 2010 and CLI Forest

Site Index. Importantly, both variables contain latent information on disturbance legacies as well as regional climate and soil patterns.

Using only the above two predictor variables, multiple-linear regression showed model performance comparable with substantially more complex models (Table 2). Multiple-linear regression model robustness was tested for the two predictor variables by performing 10-fold cross-validation repeated three times (R^2 = 0.938; RMSE = 0.079), yielding only marginally diminished model performance compared to step-wise AIC or BIC model selection models using many variables.

Table 2. Multiple linear regression model; LC = landcover; coefficients shown for variables; standard error shown in parentheses; ACC ($1 - P_o$) is the dependent variable

Independent variables	*Dependent variable*
CLI Forest Site Index	ACC ($1 - P_o$)
ABMI LC Class 2	-0.126^{***}
	(0.002)
ABMI LC Class 3	0.003
	(0.011)
ABMI LC Class 4	0.020
	(0.016)
ABMI LC Class 5	-0.185^{***}
	(0.007)

ABMI LC Class 6	-0.571***
	(0.014)
ABMI LC Class 7	-0.157***
	(0.017)
ABMI LC Class 8	-0.378***
	(0.034)
ABMI LC Class 9	-0.252***
	(0.010)
ABMI LC Class 10	-0.504***
	(0.012)
ABMI LC Class 11	-0.126***
	(0.032)
Constant	0.882***
	(0.007)
N	900
R^2	0.938
Adjusted R^2	0.938
Residual Std. Error	0.075 (df = 888)
F-Statistic	1,350.077*** (df = 10; 889)
Note:	$^{*}p$<0.1; $^{**}p$<0.05; $^{***}p$<0.01

A Random Forest regression model using all 59 predictor variables, trained with 10-fold cross-validation repeated three times, only marginally improved upon multiple-linear regression with two variables (R^2 = 0.944; RMSE = 0.070), despite a substantial increase in model complexity. Three predictors showed particularly high Random Forest variable importance (Figure 2): percent conifer, CLI forest site index, and ABMI Landcover 2010.

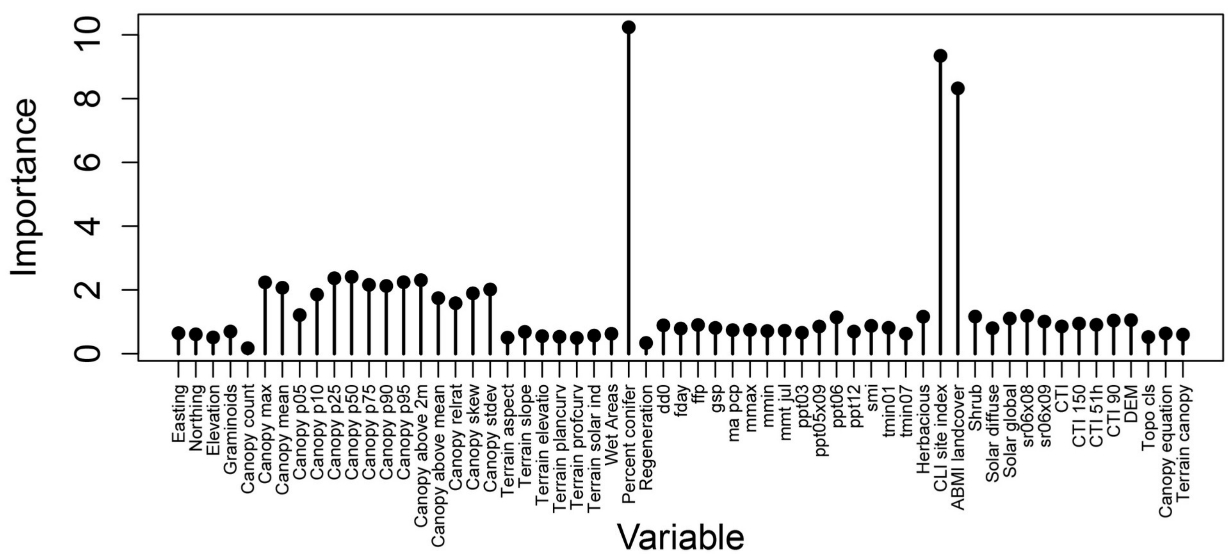

Figure 2. Random Forest variable importance (decrease in node impurities) used for initial feature selection

While percent conifer shows the highest variable importance, better Random Forest model fit was achieved with the two predictors used in multiple linear regression: CLI forest site index (productivity) and ABMI Landover 2010 class. 10-fold cross-validation was again repeated three times to assess Random Forest model performance. Random Forest models including all three variables of the highest importance explained 93.2% of variance, while models including only the CLI and ABMI landcover variables explained 93.6% of variance. For the final two-parameter Random Forest model (R^2 = 0.936; RMSE = 0.076), the scale-free variable importance of the two predictors was 18 for CLI forest site index and 68 for ABMI Landcover 2010. Thus, landcover class is inferred to be the most important predictor tested for P_o, even though Random Forest is shown to be biased toward both continuous and many-predictor categorical variables (Strobl, Boulesteix, Zeileis, & Hothorn, 2007), which may be corrected with one-hot encoding, a binary class membership scheme. We proceed by applying models using only CLI site index and ABMI landcover class as predictors. The final two-parameter Random Forest model showed reliably low error using an *n-tree* parameter of 500, or a forest of 500 decision trees for averaging (Figure 3).

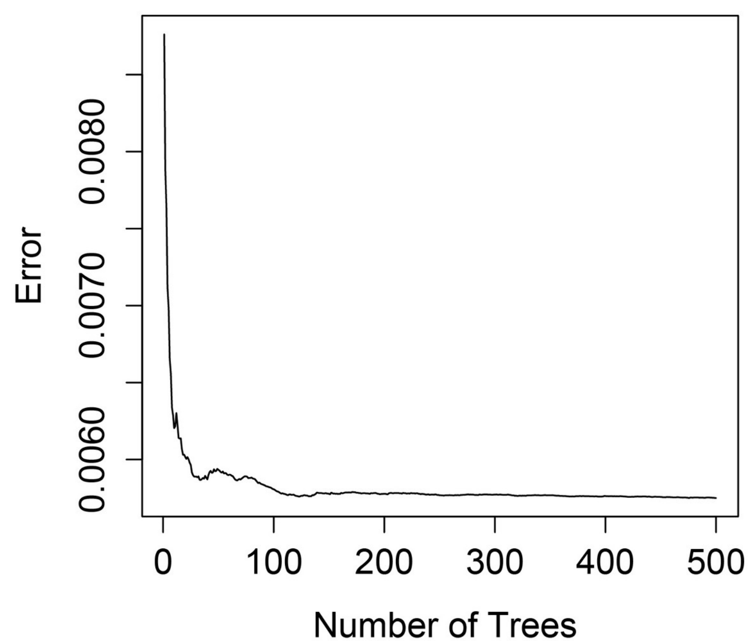

Figure 3. Random Forest model out-of-bag MSE (Error) by the number of trees parameter

Despite the strong performance of the final two-parameter Random Forest model (R^2 = 0.939; RMSE = 0.074), multiple-linear regression produced only slightly diminished model fit

(R^2 = 0.938; RMSE = 0.079) while being simpler and smaller model that is faster to apply for inference. The multivariate linear regression model also did not suffer from the bias of the Random Forest model, which tended to underpredict P_o maxima. Hence, the two-parameter multiple-linear regression model was selected as the final model for simulating P_o at the landscape-scale by applying the ABMI landcover classification scheme to simulated annual species-age cohorts to generate predictors. We simulated annual P_o by using the multiple-linear regression model for inference with dynamic simulated landcover classes and a static CLI forest site index map to generate maps of understory global solar irradiation as the multiple of canopy gap fraction and bare-Earth global solar irradiation ($P_o * I_{global}$).

The greatest variation in global solar irradiation values were shown for the Rocky Mountain and foothills regions, attributable to local topographic variation. The foothills region is characterized by the highest forest productivity in the region, while the Rocky Mountain region has moderate levels of productivity. These patterns are important for understanding the following results on modeling understory solar irradiation.

Hybrid simulations of P_o and I_u

Using the final two-parameter multiple-linear regression model with CLI forest site index and the ABMI Landcover 2010 classification scheme applied to simulated species-age cohorts, we simulated P_o at the landscape scale (25.2 million ha) and stand resolution (1 ha) with an annual time-step for a 50-year duration. Annual understory solar irradiation (Wh m^{-2} year^{-1}), or I_u, is computed by multiplying each annual map of mean simulated P_o against bare-Earth mean global solar irradiation, following a recent approach (Bode, Limm, Power, & Finlay, 2014). To plot landscape changes in I_u over time for each scenario, mean annual understory solar irradiation

($\overline{I}_u$) is computed across all forested pixels/sites at each timestep (Figure 4). Our results for each scenario show that simulated changes to $\overline{I}_u$ reflect changes to disturbance and climate over the past 90 years, in support of our main hypothesis.

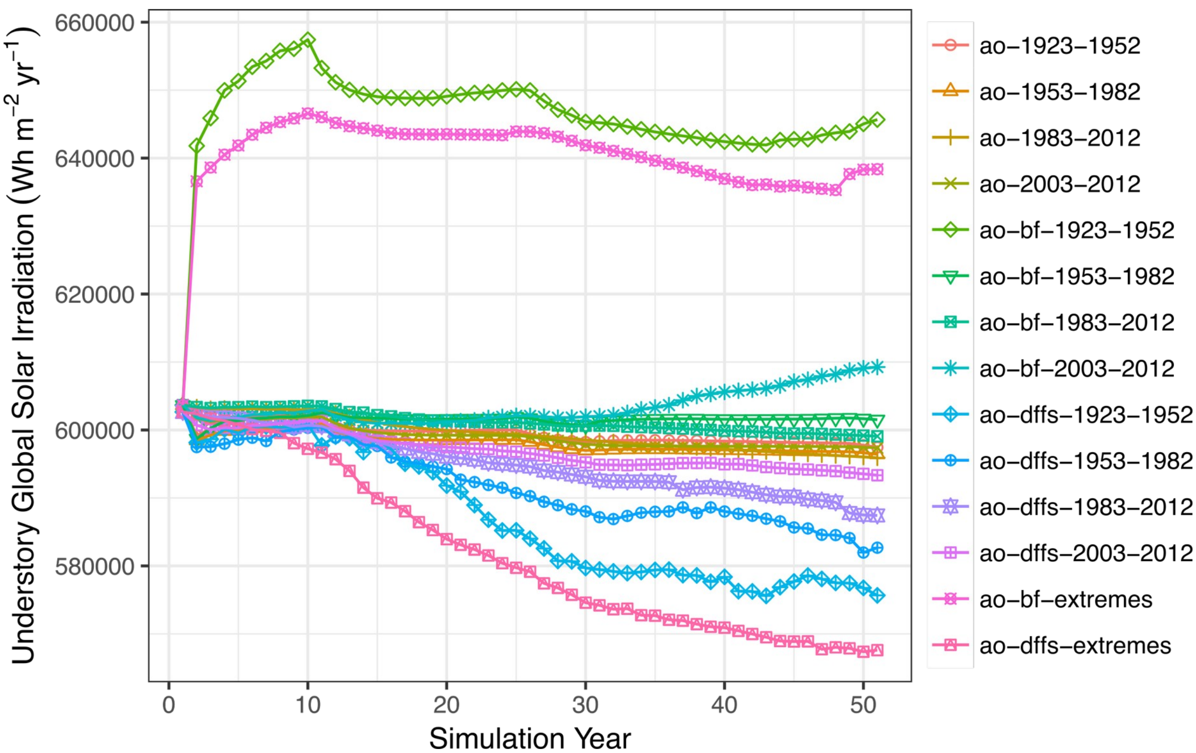

Figure 4. Simulation of mean landscape full-spectrum understory solar irradiation ($\overline{I}_u$) for forested cells in the study area for each of the fourteen model scenarios; the legend text format is as follows: [succession model]-[fire model]-[start year]-[end year]; ao = age-only succession; bf = base fire; dffs = dynamic fuels and fire system; extremes = 1923-1952 period fire (most severe) with 1983-2012 period climate (warmest)

Scenarios with severe Pre-suppression Era (1923-1952) fires show an initial rapid increase in $\overline{I}_u$ during the model spin-up decade. Meanwhile, all other simulation scenarios show a decline in $\overline{I}_u$ due to demographic changes, as stand development outweighed mortality given less severe disturbances. Absent disturbance, the effects of changes in regeneration on stand composition remain a latent process. Simulated reductions to the mean area burned and total area burned, due to fire suppression in recent decades, reduced mean understory light by a maximum of 8%, attributable to a demographic shift toward older stands. Meanwhile, higher burn rates generally produced higher landscape levels of $\overline{I}_u$.

Base Fire (*bf*) model simulations, which lack any realistic physical constraints, are notable for showing the highest landscape levels of $\overline{I}_u$. Meanwhile, semi-mechanistic Dynamic Fuels and Fire System (*dffs*) model simulations produced substantially lower levels of $\overline{I}_u$ even when parameterized with the same empirical fire regimes. This is due to process constraints built into the *dffs* fire model; large fires were followed by fuel limitations. The *dffs* model simulations yielded reduced mean $\overline{I}_u$ compared to age-only succession (*ao*) scenarios, while the lowest simulated levels of $\overline{I}_u$ were found in the *ao-dffs-extremes* scenario (Figure 5).

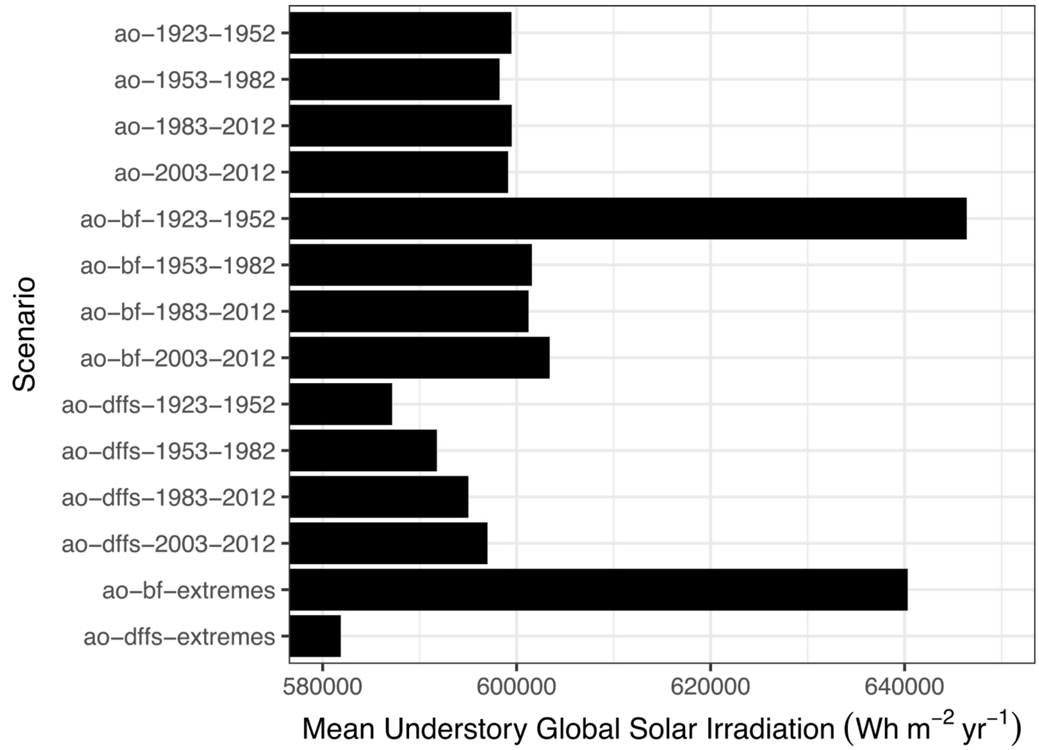

Figure 5. Mean understory solar irradiation ($\overline{I_u}$) across all simulation years by scenario; scenario naming conventions follow those of Figure 4

Reduced landscape $\overline{I_u}$ produced in the *ao-dffs-extremes* scenario may be explained by forest expansion following initial large disturbances, after which fire regimes were strongly constrained. Fuel-constrained disturbance regimes are apparent for all *dffs* scenarios (Figure 6). The *bf* scenarios, which forced the application of historical disturbance regimes without fuel or weather limitations, showed an increase in $\overline{I_u}$ for all model scenarios, except for the Early Suppression (1953-1982) and Global Change (1983-2012) Eras. During these two eras, stand development outweighed empirical fire regimes, reducing $\overline{I_u}$. In the Most Recent Decade (2003-2012) *bf* scenario, $\overline{I_u}$ increased with the rise in fire frequency, despite diminished mean fire size.

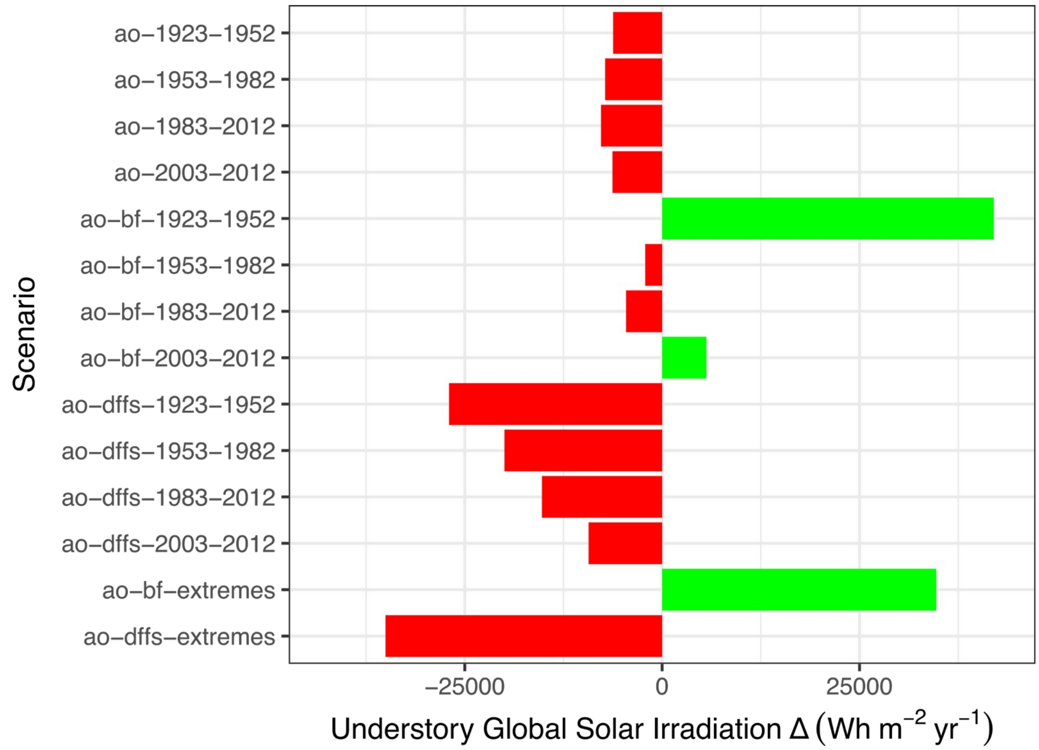

Figure 6. Change in understory solar irradiation ($\overline{I}_u$) between simulation years 0 and 50 by scenario; the scenario naming conventions again follow Figure 4

Discussion

In this study, ALS plot data were discarded as predictors of P_o due to the temporal mismatch between ALS sorties and ground validation data collection. Due to this mismatch, forest disturbance and subsequent recovery broke down the correlation structure between the two datasets. Nevertheless, ALS remains an important predictor of P_o due to its broad sampling capabilities, which are estimated to provide a more accurate and complete depiction of forest geometry. Where high point-density or waveform ALS data is available, such data is preferable to coarse traditional ground measurements.

Forest stand age, modeled implicitly in LANDIS-II simulations, plays a central role in landscape levels of $\overline{I}_u$. Higher historical burn rates produced higher levels of $\overline{I}_u$ in simulations, as mean forest age declined with higher rates of burning. The inclusion of semi-empirical fuel, temperature, and precipitation limitations in fire models notably limited the continuation of high rates of burning over multiple decades. Whether fuel and weather conditions currently impose a fundamental energetic limit on the burn rate requires further research.

The two extreme scenarios yielded divergent responses in landscape $\overline{I_u}$ depending on the fire model used, due to the inclusion of constraints in the *dffs* fire model. It is logical that a decline in forest cover may drive a long-term increase in landscape $\overline{I_u}$, if stands fail to regenerate and/or disturbance regimes become more severe under warming. In the absence of fire-related mortality, a long-term decline in regeneration rates may overcome stand aging to shift forest composition. As the simulations do not include harvest, its contribution to mortality may energetically balance the recent decline in area burned. The interaction of harvest, fire, and biological disturbance is the subject of future research. In our simulations, conversion from forestland to grasslands/shrublands due to reduced regeneration rates was caused by modeled soil water limitations (Adam M. Erickson et al., 2015). Given the importance of regeneration to our study results, the TACA model would benefit from more extensive regional validation in future studies. Given the complexity of the TACA model, requiring many difficult-to-source species-specific parameters, it would greatly benefit from model reduction strategies, as has been done for the SORTIE model in work on the Perfect Plasticity Approximation (Strigul, Pristinski, Purves, Dushoff, & Pacala, 2008).

Annual bare-Earth global solar radiation and CLI forest site index were static for each site, making $\overline{I_u}$ variation purely a function of simulated landcover change and modeled P_o. Forest demography is not explicitly modeled in the calculation of P_o. Immature trees less than ten years of age were omitted, due to a negligible effect on overstory P_o conditions and no effect of competition on regeneration. Hence, the effect of new forest growth is not apparent until ten years after disturbance. This produces a lag in $\overline{I_u}$ values and does not explain the observed simulation patterns.

Modeled landscape $\overline{I_u}$ showed divergent responses to changing fire and climate conditions. Modeled $\overline{I_u}$ indicated that understory light levels were highest under greater burn rates and warmer climatic conditions, where regeneration rates were lowest. Yet, this result depends on the type of fire model applied. We suggest applying empirical fire models for simulating well-described historical fire regimes, particularly if there is an absence of empirical support for the application of complex semi-mechanistic fire models. Studies concerned with forecasting into novel conditions may benefit from the mechanistic constraints of complex fire models, allowing theoretically robust extrapolation.

Here, our primary concern was replicating the continuation of recent historical fire patterns for modeling changes to canopy light transmission (T), a task for which both fire models provide useful information. Future studies should extend forest ecosystem simulations over century timescales to test for forest cover or compositional change, as model behavior may overcome initial landscape parameterization at century timescales, resulting in equilibrium or stability conditions. Yet, model uncertainty also increases with longer simulation timescales through error propagation, motivating our use of half-century simulations. Regardless of temporal scale, most critical are the simulation time-points where regime shifts are likely to occur, which signify transitions in the state-space of forests. By combining remote sensing with simulation models, dedicated state-space models designed for linear systems with random disturbances, such as the Extended Kalman filter (Kalman & Bucy, 1961), may be used to better understand the recent historical state of forest ecosystems.

Evidence is provided that a diminished rate of burning likely decreased $\overline{I_u}$ in recent years, attributable to a demographic shift occurring through stand development processes in the absence of fire-related mortality. This is supported by a precursory analysis of Alberta Permanent Sample Plot data for the region (Adam Michael Erickson, 2017), which showed a reduction in regeneration and mean tree height – inferred to correspond to a reduction in mean tree age – across the Global Change Era. Future studies should incorporate the effects of harvest and biological disturbance agents with more sophisticated succession models to estimate the effects of each on understory light levels, while further incorporating remote sensing data through a state-space modeling framework.

Limitations

Here, a physical solar radiation model was combined with a regression model of P_o using forest site index and simulated landcover as predictors. The layering of these models may produce error propagation, common to complex models lacking global parameter optimization (Pacala et al., 1996; Arras, 1998; Larocque, Bhatti, Boutin, & Chertov, 2008). These uncertainties were not explicitly represented given the complexity of the models and scope of this research. Additionally, the solar radiation model used assumes constant solar output, which is known to be false, but is a reasonable assumption given that work is not concerned with temporal variation in solar activity. Other limitations of the solar radiation model include its reliance on simple geometric relationships and lack of radiative transfer functions related to turbidity or cloud cover.

Of these shortcomings, the absence of cloud cover information is expected to have the largest effect on modeled radiation, as clouds may be the largest source of radiation attenuation in the atmosphere (Hammer et al., 2003). Cloud cover indices derived from geostationary weather satellite data may be used to generate atmospheric clearness indices. Such indices facilitate a simple but effective method of integrating spatiotemporally resolved atmospheric conditions with models of clear-sky solar radiation and LiDAR canopy light transmission (Tooke, Coops, Christen, Gurtuna, & Prévot, 2012). Finally, while changes to landcover were dynamically simulated, forest site index was static (Agriculture and Agri-Food Canada, 2016). Future studies should test the application of NDVI, NIR_V, or SIF for incorporating dynamic changes to stand productivity or site index.

Conclusion

Here, we developed and demonstrated the first hybrid vegetation model using machine learning. Ultimately though, a multiple-linear regression model showed comparable performance at reduced complexity and computational cost. Our hybrid model simulations showed that I_u levels increased under Pre-suppression Era and Most Recent Decade conditions using the statistical fire model. Yet, I_u levels declined in all other scenarios. The choice of fire model was a key differentiator in model results. Using the extremes scenarios as an example, where the warmest climate conditions were applied with the most severe burn rates, I_u levels substantially increased with the statistical fire model and decreased with the semi-mechanistic fire model over the 50-year simulation period. In all other scenarios, the recruitment of new cohorts and stand development outweighed disturbance-related mortality, producing stand ageing and a mean decline in I_u levels. Importantly, the resulting annual one-hectare maps of simulated I_{global} faithfully captured the ‘feast-or-famine’ light conditions of montane regions in the study area, due to topographic position effects (i.e., slope and azimuth).

The simple statistical fire model consistently produced the parameterized fire regime without constraint, while the semi-mechanistic fire model was strongly constrained by fuel and weather limitations. The appropriate choice of fire model depends strongly on the research question. This work applied both types of fire model in an effort to better understand forest ecosystem trajectories using ensembles based on unique scenarios. Applying the statistical fire model with empirical parameters, it was clear that weakened disturbance regimes reduced modeled I_u across the landscape. However, the past decade showed an increase in the rate of burning and thus in I_u, attributable to exponentially increased fire frequency linked to an increase in human activity in previously remote areas (Adam Michael Erickson, 2017). These results may be indicative of future national fire regimes as population levels and temperatures continue to rise throughout the circumpolar boreal zone, with the southern reaches of these forests likely the first to experience compositional and anthropogenic changes.

Acknowledgements

We thank funders and collaborators for making this work possible. A.E. and N.C. were funded by Foothills Research Association’s Grizzly Bear Program and an NSERC grant to N.C. A.E. proposed and implemented the presented methodology, and, led the writing of the manuscript. N.C. managed the overall research and contributed to the writing. C.N. provided TACA model parameters to conduct the regeneration modeling work and contributed to the writing. G.S. provided the necessary regional expertise and support to conduct this research.

References

Agriculture and Agri-Food Canada. (2016). Canada Land Inventory (CLI). Retrieved 1 January 2015, from http://sis.agr.gc.ca/cansis/nsdb/cli/index.html

Alberta Biodiversity Monitoring Institute. (2012). *ABMI Wall-to-wall Land Cover Map circa 2000, Version 2.1: Metadata*. Edmonton, AB, Canada: Alberta Biodiversity Monitoring Institute. Retrieved from http://ftp.public.abmi.ca//GISData/LandCover/W2W2000/ABMIw2wLCV2000v2.1 Metadata.pdf

Arp, P., Castonguay, M., Campbell, D., & Hiltz, D. (2009). *Overview of wet-areas mapping and industry applications*. Fredericton, NB, USA: University of New Brunswick. Retrieved from http://watershed.for.unb.ca/files/alberta_wam.pdf

Arras, K. O. (1998). *An introduction to error propagation: derivation, meaning and examples of equation CY = FX CX FXT*. Lausanne, Switzerland. Retrieved from http://www2.informatik.uni-freiburg.de/~arras/papers/arrasTR98.pdf

Aubin, I., Beaudet, M., & Messier, C. (2000). Light extinction coefficients specific to the understory vegetation of the southern boreal forest, Quebec. *Canadian Journal of Forest Research*, *30*(1), 168–177. doi:10.1139/x99-185

Bartemucci, P., Messier, C., & Canham, C. D. (2006). Overstory influences on light attenuation patterns and understory plant community diversity and composition in southern boreal forests of Quebec. *Canadian Journal of Forest Research*, *36*(9), 2065–2079. doi:10.1139/x06-088

Beaudet, M., Harvey, B. D., Messier, C., Coates, K. D., Poulin, J., Kneeshaw, D. D., … Bergeron, Y. (2011). Managing understory light conditions in boreal mixedwoods through variation in the intensity and spatial pattern of harvest: A modelling approach. *Forest Ecology and Management*, *261*(1), 84–94. doi:http://dx.doi.org/10.1016/j.foreco.2010.09.033

Beaudet, M., & Messier, C. (2002). Variation in canopy openness and light transmission following selection cutting in northern hardwood stands: an assessment based on hemispherical photographs. *Agricultural and Forest Meteorology*, *110*(3), 217–228. doi:http://dx.doi.org/10.1016/S0168-1923(01)00289-1

Bode, C. A., Limm, M. P., Power, M. E., & Finlay, J. C. (2014). Subcanopy solar radiation model: Predicting solar radiation across a heavily vegetated landscape using LiDAR and GIS solar radiation models. *Remote Sensing of Environment*, *154*, 387–397. doi:http://dx.doi.org/10.1016/j.rse.2014.01.028

Breiman, L. (1996). Bagging Predictors. *Machine Learning*, *24*.

Breiman, Leo. (2001). Random Forests. *Machine Learning*, *45*(1), 5–32. doi:10.1023/A:1010933404324

Canham, C. D., Finzi, A. C., Pacala, S. W., & Burbank, D. H. (1994). Causes and consequences of resource heterogeneity in forests: interspecific variation in light transmission by canopy trees. *Canadian Journal of Forest Research*, *24*(2), 337–349. doi:10.1139/x94-046

Chazdon, R. L., & Pearcy, R. W. (1991). The Importance of Sunflecks for Forest Understory Plants. *BioScience*, *41*(11), 760–766. Retrieved from http://www.jstor.org/stable/1311725

D'Orangeville, L., Houle, D., Duchesne, L., Phillips, R. P., Bergeron, Y., & Kneeshaw, D. (2018). Beneficial effects of climate warming on boreal tree growth may be transitory. *Nature Communications*, *9*(1), 3213. doi:10.1038/s41467-018-05705-4

Dengel, S., & Grace, J. (2010). Carbon dioxide exchange and canopy conductance of two coniferous forests under various sky conditions. *Oecologia*, *164*(3), 797–808. doi:10.1007/s00442-010-1687-0

Enquist, B. J., & Niklas, K. J. (2001). Invariant scaling relations across tree-dominated communities. *Nature*, *410*(6829), 655–60. doi:10.1038/35070500

Enquist, B. J., West, G. B., & Brown, J. H. (2009). Extensions and evaluations of a general quantitative theory of forest structure and dynamics. *Proc Natl Acad Sci*, *106*.

Erickson, Adam M., Nitschke, C. R., Coops, N. C., Cumming, S. G., & Stenhouse, G. B. (2015). Past-century decline in forest regeneration potential across a latitudinal and elevational gradient in Canada. *Ecological Modelling*, *313*, 94–102. doi:http://dx.doi.org/10.1016/j.ecolmodel.2015.06.027

Erickson, Adam Michael. (2017). *A hybrid modeling approach to simulating past-century understory solar irradiation in Alberta, Canada* (Electronic Theses and Dissertations (ETDs) 2008+). University of British Columbia. doi:/http://dx.doi.org/10.14288/1.0354540

Farquhar, G. ~D., & Roderick, M. ~L. (2009). Evaporative demand, transpiration, and photosynthesis: How are they changing? In D. ~N. Arabelos & C. ~C. Tscherning (Eds.), *EGU General Assembly Conference Abstracts* (Vol. 11, p. 13537).

Fu, P., & Rich, P. (1999). Design and implementation of the Solar Analyst: An ArcView extension for modeling solar radiation at landscape scales. In *Proceedings of the 19th Annual ESRI User Conference* (p. 33). San Diego, CA, USA: ESRI. Retrieved from http://professorpaul.com/publications/fu_rich_1999_esri.pdf

Fu, P., & Rich, P. M. (2002). A geometric solar radiation model with applications in agriculture and forestry. *Computers and Electronics in Agriculture*, *37*(1–3), 25–35. doi:http://dx.doi.org/10.1016/S0168-1699(02)00115-1

Grandin, U. (2004). Dynamics of understory vegetation in boreal forests: experiences from Swedish integrated monitoring sites. *Forest Ecology and Management*, *195*(1–2), 45–55. doi:http://dx.doi.org/10.1016/j.foreco.2004.02.053

Greene, D. F., Zasada, J. C., Sirois, L., Kneeshaw, D., Morin, H., Charron, I., & Simard, M.-J. (1999). A review of the regeneration dynamics of North American boreal forest tree species. *Canadian Journal of Forest Research*, *29*(6), 824–839. doi:10.1139/x98-112

Hammer, A., Heinemann, D., Hoyer, C., Kuhlemann, R., Lorenz, E., Müller, R., & Beyer, H. G. (2003). Solar energy assessment using remote sensing technologies. *Remote Sensing of Environment*, *86*(3), 423–432. doi:http://dx.doi.org/10.1016/S0034-4257(03)00083-X

Hastie, T., Tibshirani, R., & Friedman, J. (2009). *Elements of Statistical Learning: Data Mining, Inference, and Prediction* (2nd ed.). New York, NY, USA: Springer-Verlag. doi:10.1007/978-0-387-84858-7

He, T., Pausas, J. G., Belcher, C. M., Schwilk, D. W., & Lamont, B. B. (2012). Fire-adapted traits of Pinus arose in the fiery Cretaceous. *New Phytologist*, *194*(3), 751–759. doi:10.1111/j.1469-8137.2012.04079.x

Hikosaka, K., & Hirose, T. (1997). Leaf angle as a strategy for light competition: Optimal and evolutionarily stable light-extinction coefficient within a leaf canopy. *Ecoscience*, *4*(4), 501–507. Retrieved from http://www.jstor.org/stable/42902397

Iqbal, M. (1983). *An Introduction To Solar Radiation* (1st ed.). Amsterdam, Netherlands: Elsevier Science. Retrieved from https://books.google.de/books?id=3_qWce_mbPsC

Kalman, R. E., & Bucy, R. S. (1961). New results in linear filtering and prediction theory. *Journal of Basic Engineering*, *83*(1), 95–108. Retrieved from http://dx.doi.org/10.1115/1.3658902

Katahata, S., Naramoto, M., Kakubari, Y., & Mukai, Y. (2005). Photosynthetic acclimation to dynamic changes in environmental conditions associated with deciduous overstory phenology in Daphniphyllum humile, an evergreen understory shrub. *Tree Physiology* , *25*(4), 437–445. doi:10.1093/treephys/25.4.437

Larocque, G. R., Bhatti, J. S., Boutin, R., & Chertov, O. (2008). Uncertainty analysis in carbon cycle models of forest ecosystems: Research needs and development of a theoretical framework to estimate error propagation. *Ecological Modelling*, *219*(3), 400–412. doi:http://dx.doi.org/10.1016/j.ecolmodel.2008.07.024

Laskin, D. N., Montaghi, A., Nielsen, S. E., & McDermid, G. J. (2016). Estimating Understory Temperatures Using MODIS LST in Mixed Cordilleran Forests. *Remote Sensing, 8*(8). doi:10.3390/rs8080658

Lieffers, V. J., Messier, C., Stadt, K. J., Gendron, F., & Comeau, P. G. (1999). Predicting and managing light in the understory of boreal forests. *Canadian Journal of Forest Research, 29*(6), 796–811. doi:10.1139/x98-165

McGaughey, R. J. (2014). FUSION/LDV: Software for LiDAR data analysis and visualization. Seattle, USA: US Department of Agriculture, Forest Service. Retrieved from http://forsys.cfr.washington.edu/fusion/fusionlatest.html

Nielsen, S. E. (2005). *Habitat ecology, conservation, and projected population viability of grizzly bears (Ursus Arctos L.) in west-central Alberta, Canada*. University of Alberta, Edmonton, AB, Canada. Retrieved from https://sites.ualberta.ca/~scottn/documents/NielsenPhDa.pdf

Nilsson, M.-C., & Wardle, D. A. (2005). Understory vegetation as a forest ecosystem driver: evidence from the northern Swedish boreal forest. *Frontiers in Ecology and the*

Environment, *3*(8), 421–428. doi:10.1890/1540-9295(2005)003[0421:UVAAFE]2.0.CO;2

Nitschke, C. R., & Innes, J. L. (2008). A tree and climate assessment tool for modelling ecosystem response to climate change. *Ecological Modelling*, *210*(3), 263–277. doi:10.1016/j.ecolmodel.2007.07.026

Pacala, S. W., Canham, C. D., Saponara, J., Silander, J. A., Kobe, R. K., & Ribbens, E. (1996). Forest models defined by field measurements: estimation, error analysis and dynamics. *Ecological Monographs*, *66*(1), 1–43. doi:10.2307/2963479

Pec, G. J., Karst, J., Sywenky, A. N., Cigan, P. W., Erbilgin, N., Simard, S. W., & Cahill Jr., J. F. (2015). Rapid Increases in Forest Understory Diversity and Productivity following a Mountain Pine Beetle (Dendroctonus ponderosae) Outbreak in Pine Forests. *PLOS ONE*, *10*(4), 1–16. doi:10.1371/journal.pone.0124691

Reich, P. B., Frelich, L. E., Voldseth, R. A., Bakken, P., & Adair, E. C. (2012). Understorey diversity in southern boreal forests is regulated by productivity and its indirect impacts on resource availability and heterogeneity. *Journal of Ecology*, *100*(2), 539–545. doi:10.1111/j.1365-2745.2011.01922.x

Rich, P. M., Dubayah, R., Hetrick, W. A., & Saving, S. C. (1994). Using viewshed models to calculate intercepted solar radiation: Applications in ecology. *American Society for Photogrammetry and Remote Sensing Technical Papers*, 524–529.

Rich, Paul M. (1990). Characterizing plant canopies with hemispherical photographs. *Remote Sensing Reviews*, *5*(1), 13–29. doi:10.1080/02757259009532119

Rowe, J. S. (1973). Fire in the Boreal, *444464*.

Rowe, J. S., & Scotter, G. W. (1973). Fire in the boreal forest. *Quaternary Research*, *3*(3), 444–464. doi:http://dx.doi.org/10.1016/0033-5894(73)90008-2

Ruban, A. V. (2009). Plants in light. *Communicative & Integrative Biology*, *2*(1), 50–55. doi:10.4161/cib.2.1.7504

Scheller, R. M., Domingo, J. B., Sturtevant, B. R., Williams, J. S., Rudy, A., Gustafson, E. J., & Mladenoff, D. J. (2007). Design, development, and application of LANDIS-II, a spatial landscape simulation model with flexible temporal and spatial resolution. *Ecological Modelling*, *201*(3–4), 409–419. doi:10.1016/j.ecolmodel.2006.10.009

Strigul, N., Pristinski, D., Purves, D., Dushoff, J., & Pacala, S. (2008). Scaling from trees to forests: tractable macroscopic equations for forest dynamics. *Ecological Monographs*, *78*(4), 523–545. doi:10.1890/08-0082.1

Strobl, C., Boulesteix, A.-L., Zeileis, A., & Hothorn, T. (2007). Bias in random forest variable importance measures: illustrations, sources and a solution. *BMC Bioinformatics*, *8*(1), 1–21. doi:10.1186/1471-2105-8-25

Šúri, M., & Hofierka, J. (2004). A new GIS-based solar radiation model and its application to photovoltaic assessments. *Transactions in GIS*, *8*(2), 175–190. doi:10.1111/j.1467-9671.2004.00174.x

Tooke, T. R., Coops, N. C., Christen, A., Gurtuna, O., & Prévot, A. (2012). Integrated irradiance modelling in the urban environment based on remotely sensed data. *Solar Energy*, *86*(10), 2923–2934. doi:http://dx.doi.org/10.1016/j.solener.2012.06.026

Trenberth, K. E. (2011). Changes in precipitation with climate change. *Climate Research*, *47*(1–2), 123–138. Retrieved from http://www.int-res.com/abstracts/cr/v47/n1-2/p123-138/

Wang, T., Hamann, A., Spittlehouse, D. L., & Murdock, T. Q. (2011). ClimateWNA: High-resolution spatial climate data for western North America. *Journal of Applied Meteorology and Climatology*, *51*(1), 16–29. doi:10.1175/JAMC-D-11-043.1

Way, D. A., & Pearcy, R. W. (2012). Sunflecks in trees and forests: from photosynthetic physiology to global change biology. *Tree Physiology*, *32*(9), 1066–1081. doi:10.1093/treephys/tps064

Widrow, B., & Hoff, M. (1960). *Adaptive switching circuits*. *Technical Report Number 1553-1*. Stanford, California: Stanford University, Stanford Electronics Laboratory. Retrieved from http://www-isl.stanford.edu/~widrow/papers/c1960adaptiveswitching.pdf

Wright, I. J., Reich, P. B., Westoby, M., Ackerly, D. D., Baruch, Z., Bongers, F., … Villar, R. (2004). The worldwide leaf economics spectrum. *Nature*, *428*, 821. Retrieved from https://doi.org/10.1038/nature02403

Supplementary Material

In the following section, we describe the simulation scenario codes used throughout this study (Table S1), the soil parameters used in TACA-EM (Table S2), the tree species biophysical parameters used in TACA-EM (Table S3), and the tree species life history attribute parameters used in the LANDIS-II model (Table S4). For further information on model parameterization, please refer to our openly available parameter files (https://github.com/adam-erickson/ML-FEM) and to a parallel study currently in review (available on request from the corresponding author).

Table S1. Simulation scenario codes based on model configuration and period

LANDIS-II Configuration	Period	Abbreviation
Age-only succession	1923-1952	ao-1923-1952
Age-only succession	1953-1982	ao-1953-1982
Age-only succession	1983-2012	ao-1983-2012
Age-only succession	2003-2012	ao-2003-2012
Age-only succession with base fire	1923-1952	ao-bf-1923-1952
Age-only succession with base fire	1953-1982	ao-bf-1953-1982
Age-only succession with base fire	1983-2012	ao-bf-1983-2012
Age-only succession with base fire	2003-2012	ao-bf-2003-2012
Age-only succession with dynamic fire	1923-1952	ao-dffs-1923-1952
Age-only succession with dynamic fire	1953-1982	ao-dffs-1953-1982
Age-only succession with dynamic fire	1983-2012	ao-dffs-1983-2012
Age-only succession with dynamic fire	2003-2012	ao-dffs-2003-2012
Age-only succession with base fire	Extremes	ao-bf-extremes
Age-only succession with dynamic fire	Extremes	ao-dffs-extremes

Table S2. Soils parameters used in TACA-EM

Natural Subregion	Soil Texture	Rooting Zone Depth (m)	Coarse Fragment %	AWSC (mm/m)	Field Capacity (mm/m)	Percolation (mm/day)	Latitude
Alpine	-	-	-	-	-	-	-
Central Mixedwood	SiCL	1.0	5%	452	560	93.1	55˚
Central Parkland	CL	1.0	5%	341	470	122.6	50˚
Dry Mixedwood	CL	1.0	5%	341	470	122.6	55˚
Foothills Fescue	CL	1.0	5%	341	470	122.6	50˚
Foothills Parkland	CL	1.0	20%	341	470	103.2	50˚
Lower Boreal Highlands	CL	1.0	20%	341	470	103.2	55˚
Lower Foothills	CL	1.0	5%	341	470	122.6	55˚
Mixedgrass	CL	1.0	5%	341	470	122.6	50˚
Montane	L	1.0	20%	377	460	66.4	50˚
Peace River Parkland	CL	1.0	5%	341	470	122.6	55˚
Subalpine	L	1.0	20%	377	460	66.4	50˚
Upper Boreal Highlands	CL	1.0	20%	341	470	103.2	55˚
Upper Foothills	CL	1.0	5%	341	470	122.6	55˚

Table S3. Tree species biophysical parameters used in TACA-EM

Species	Model Code	Physiological Base Temperature (℃)	Heat Sum for Bud Burst (GDD)	Chilling Requirement (Days)	Minimum Temperature (℃)	Drought Tolerance	GDD Minimum	GDD Maximum	Frost Tolerance	Frost Season	Wet Soils	Heat Moisture Index
Abies balsamea	Sp1	2.8	121	49	-62	0.20	560.0	2,386	0.9	305	0.55	41.4
Abies lasiocarpa	Sp3	2.6	119	70	-67	0.25	197.6	5,444	0.9	320	0.75	28.7
Betula payrifera	Sp5	3.7	231	77	-80	0.30	236.8	4,122	0.9	285	0.30	40.0
Larix laricina	Sp7	2.9	111	42	-76	0.20	150.8	3,331	0.9	300	0.75	33.8
Larix occidentalis	Sp8	3.4	180	70	-40	0.40	163.2	3,057	0.7	305	0.05	38.7
Picea engelmannii	Sp9	3.1	145	49	-64	0.25	74.4	2,150	0.9	335	0.50	28.7
Picea glauca	Sp10	2.7	147	42	-69	0.34	129.6	3,459	0.9	305	0.50	43.2
Picea mariana	Sp11	3.0	123	56	-69	0.30	144.0	3,060	0.9	305	1.00	42.7
Pinus banksiana	Sp13	2.8	108	56	-85	0.50	830.0	2,216	0.9	320	0.30	37.9
Pinus contorta	Sp14	2.9	116	63	-85	0.42	185.6	3,374	0.9	320	0.50	37.9
Pinus monticola	Sp15	4.4	468	98	-85	0.25	211.2	3,554	0.75	305	0.50	25.8
Populus balsamifera	Sp17	2.1	93	49	-80	0.13	126.0	7,852	0.9	290	0.55	59.0
Populus tremuloides	Sp18	3.5	189	70	-80	0.40	226.8	4,414	0.9	284	0.30	40.0

Table S4. Tree species life history attribute parameters used in LANDIS-II

Species	Longevity	Sexual Maturity Age	Shade Tolerance	Fire Tolerance	Effective Seed Dispersal Distance	Maximum Seed Dispersal Distance	Vegetative Reproduction Probability	Sprouting Minimum Age	Sprouting Maximum Age	Post-Fire Regeneration
Abies balsamea	150	25	5	1	30	160	-1	-1	-1	None
Abies lasiocarpa	200	20	4	2	30	80	0.05	20	200	None
Betula papyrifera	150	15	2	1	100	200	0.5	1	60	Resprout
Larix laricina	150	10	1	3	38	60	0.05	10	150	None
Larix occidentalis	400	15	1	5	100	240	-1	-1	-1	None
Picea engelmannii	720	15	3	2	46	183	0.05	15	720	None

Picea glauca	350	25	3	2	100	300	0.05	25	350	None
Picea mariana	150	30	4	1	260	260	0.05	30	200	Serotiny
Pinus banksiana	200	10	2	4	37	60	-1	-1	-1	Serotiny
Pinus contorta	200	5	2	4	27	200	-1	-1	-1	Serotiny
Pinus monticola	350	7	3	3	120	800	-1	-1	-1	None
Populus balsamifera	200	9	2	3	50	3000	0.5	9	200	Resprout
Populus tremuloides	200	2	1	4	uni	5000	0.95	1	200	Resprout